



Research on the preparation and property of superhydrophobic surface with micro-nano ripple structure

Yunhu Zhu^{1,2,3} , Aixin Feng^{1,2,3,a)}, Xiaoming Pan², Jinhai Yu⁴, Pu Zhao^{1,2}

¹ Rui'an Graduate College of Wenzhou University, Wenzhou University, Wenzhou 325206, China

² College of Mechanical & Electrical Engineering, Wenzhou University, Wenzhou 325035, China

³ Zhejiang Provincial Key Laboratory of Laser Processing Robots/Key Laboratory of Laser Precision Processing & Detection, Wenzhou 325035, China

⁴ Zhejiang Jinlong Automatic Control Equipment Co., Ltd, Wenzhou 325299, China

^{a)} Address all correspondence to this author. e-mail: aixfeng@126.com

Received: 22 November 2022; accepted: 8 May 2023; published online: 6 June 2023

Superhydrophobic surfaces are widely used in various fields because of their excellent properties and are currently an important research hotspot. Here, we developed a simple method and successfully prepared a functional surface with superhydrophobic properties. The relationship between laser process parameters on the surface morphology and wettability properties of stainless steel mesh was systematically investigated, and the surface corrosion resistance, mechanical stability, and self-cleaning properties of superhydrophobic stainless steel mesh were explored. The results show that under laser ablation with optimal process parameters, the surface of the superhydrophobic SSM has a large number of laser-induced periodic micro-nano corrugated structures, which store a large amount of air in the structure to form a layer of air cushion, reducing the contact between the surface and the corrosion solution, improving the corrosion resistance of the SSM, and also showing excellent performance characteristics in terms of mechanical stability, time-sensitive, and self-cleaning performance.

Introduction

Inspired by biological surfaces such as lotus leaves [1] and water striders [2], superhydrophobic surfaces with high Water Contact angles (WCA > 150°), and low sliding angles (SA < 10°) have received much attention from academia and industry [3, 4]. Superhydrophobic surfaces have a wide range of potential applications in the fields of oil–water separation [5, 6], anti-icing [7, 8], and water collection [9, 10].

So far, many authors have used different methods to successfully prepare superhydrophobic surfaces on different material surfaces. For the preparation of superhydrophobic surfaces, two basic factors play an important role: appropriate micro-nanostructures and low surface energy. At present, the main methods for preparing superhydrophobic surfaces include electrochemical deposition [11, 12], chemical etching [13, 14], anodic oxidation [15, 16], sol–gel method [17–19], and laser ablation [20–22]. Some of these methods do not

have a strong bond between the constructed microstructure and the substrate, and the material surface is damaged by external influences (including mechanical stress and chemical contamination), which limits the application of materials whose surface microstructure is susceptible to wear and tear damage, or even fall off in. In this paper, laser ablation technology is used to construct micro- and nanostructures. Laser processing methods have gained widespread attention in recent years because of their advantages, such as high precision, high process flexibility, high automation, and low environmental pollution. Yong et al. [23] treated stainless steel mesh by femtosecond laser processing, and the mesh surface showed micro-sub-micro-nano-level structure after laser ablation and successfully prepared aerobic surface. Lian et al. [24] prepared robust microstructure on 304 stainless steel mesh (SSM-WJALA) by laser ablation technique, and single-factor testing of different laser parameters on the surface of stainless

steel mesh. Wang et al. [25] established a rough oxide coating with micro/nanoscale structure on 304 stainless steel mesh (SSM) by laser ablation and investigated the effect of a single laser parameter on the surface morphology and wettability. A review of the relevant literature shows that laser ablation of stainless steel mesh surfaces is rarely reported, and systematic studies of laser parameters on surface morphology and wettability are even less reported.

Superhydrophobic surfaces have excellent performance properties mainly including corrosion resistance [26, 27], anti-icing [28–30], and Self-cleaning stain removal [31–38]. Superhydrophobic surfaces with excellent properties can be prepared by a simple process for mass production and application. Tan et al. [39] have applied superhydrophobicity to outdoor applications, such as windshields and lenses, demonstrating excellent self-cleaning, and anti-fogging properties of superhydrophobicity. R Wu et al. [40] successfully prepared aluminum alloy surfaces with microstructures by anodic oxidation. The CA of the aluminum alloy surface after coating with polypropylene film was 154° and the SA was 3°. The corrosion resistance of the modified superhydrophobic aluminum alloy was improved compared to the aluminum coated with unmodified film. C Hu et al. [41] prepared superhydrophobic coatings on carbon steel substrates using electrodeposition, and the surfaces showed good mechanical and chemical stability based on tests of knife scratching, tape peeling, sandpaper abrasion, and chemical resistance. J Zhang et al. [42] prepared superhydrophobic ice-resistant aluminum sheets using hydrothermal method on aluminum sheets with anti-icing and self-cleaning surfaces. The need to maintain long-lasting corrosion resistance and mechanical stability properties of superhydrophobic surfaces in relevant environments is an urgent issue to be addressed.

In this paper, we propose a simple and general method to prepare superhydrophobic surfaces on SSM. The superhydrophobic surface was prepared by laser ablation of the SSM surface to form a large number of micro and nano corrugated structures and combined with stearic acid solution modification. The effect of different laser parameters (power density, scanning speed, scanning interval) on the surface morphology and wettability of the SSM was studied by the controlled variable method in the experiments. The reaction of the surface of the SSM with stearic acid and the effect of chemical elements on the wettability of the surface were studied. The electrochemical corrosion test showed that the surface of the superhydrophobic SSM has excellent corrosion resistance due to the presence of micro-nano ripple structure on the surface. After 60 days of time sensitivity and self-cleaning tests, the WCA on the surface of the superhydrophobic SSM can still reach more than 150°, which indicates that the prepared superhydrophobic SSM has good stability.

Results and discussion

Surface morphology and wettability

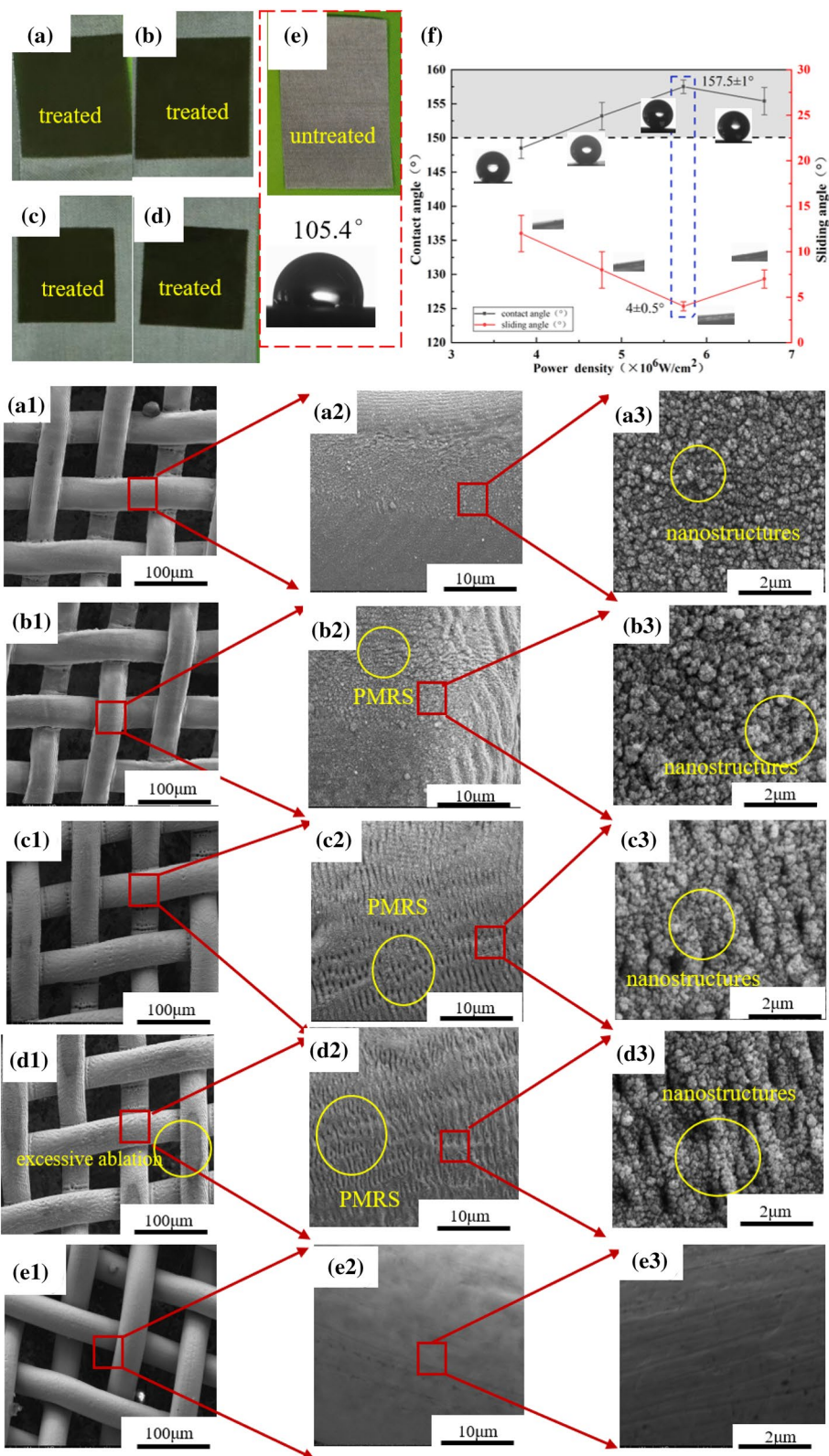
The effect of laser power density on SSM morphology and wettability

To investigate the effect of laser power density on the morphology and wettability of SSM, under the same other parameters (scanning speed of 150 mm/s, scanning interval of 20 μm), the scanning power density of 3.82×10^6 W/cm², 4.77×10^6 W/cm², 5.73×10^6 W/cm², and 6.68×10^6 W/cm² (power selected as 40%, 50%, 60%, 80%) of four sets of parameters was to prepare superhydrophobic SSM and analyze its surface morphology and wettability results.

Fig. 1(a–e) corresponds to the surface morphology of the laser power density of 3.82×10^6 W/cm², 4.77×10^6 W/cm², 5.73×10^6 W/cm², and 6.68×10^6 W/cm² and untreated macroscopic SSM with a laser scan area of 1 cm², respectively. From the figure can be seen that gray–white is for the original SSM and black belongs to the laser ablation area, which is caused by laser ablation of SSM after surface oxidation. Due to the increase in laser power density, resulting in increasing energy per unit area, making the depth of stainless steel mesh ablation increases and the color of the material surface becomes darker and darker. Figure 1(a1–a3), (b1–b3), (c1–c3), and (d1–d3) shows SEM images of the laser-ablated SSM at different magnifications. As shown in Fig. 1(a2–d2), with the increase of laser power density, the metal wire surface is covered with periodic micron ripple structure (PMRS) from scratch to existence, and the micron ripple period is about 1 μm. The PMRS is generated due to the interference between the incident laser beam and the scattered laser beam during laser ablation. Meanwhile, as shown in Fig. 1(b3–d3), on the PMRS and accompanied by the generation of nanoparticles. This is due to the emergence of nanoparticles on the PMRS by the plasma jet generated by the low power density spot edge ablation during spot movement and finally the micro-nano double-scale structure formed on the surface of the SSM, which increases the surface roughness compared to the untreated [Fig. 1(e1–e3)] surface of the SSM. Therefore, this micro-nano double-scale structure is formed by the uneven distribution of laser power density of the laser spot and the motion of the laser spot. When the laser power density is lower than 3.82×10^6 W/cm², only nanoparticles will appear on the surface of the SSM and no PMRS will appear.

In order to investigate the relationship between surface morphology and wetting properties, we also measured the WCA and SA of the surface of SSM modified by stearic acid at different laser power densities. Figure 1(f) shows the plot of WCA and SA versus laser power density. The SSM surfaces under four sets of laser parameter ablation and after stearic acid modification have hydrophobic properties with WCA exceeding 145°,

Figure 1: The relationship between power density and surface morphology and WCA. (a–e) The macroscopic surface morphology of laser-ablated SSM at different power densities; (a1–e1), (a2–e2), and (a3–e3) are the microscopic SEM of laser-ablated SSM at different power densities with magnifications of $\times 1000$, $\times 10000$, and $\times 50000$, respectively.



partially reaching superhydrophobicity. With the increase in power density WCA increases SA decreases, when the power density of $5.73 \times 10^6 \text{ W/cm}^2$, at this time reached the optimal

performance, WCA of $157.5 \pm 1^\circ$ and SA of $4 \pm 0.5^\circ$. When the power density is higher than $5.73 \times 10^6 \text{ W/cm}^2$, as the power density increases the WCA decreases the SA increases. The

surface of the laser-ablated and stearic acid-modified SSM exhibits hydrophobicity and with the increase of power density leads to the generation of PMRS, which increases the roughness of the surface and makes the WCA of the surface increase continuously. However, the laser power density is higher than $5.73 \times 10^6 \text{ W/cm}^2$, as shown in Fig. 1(d1), laser over-ablation of the SSM surface destroyed part of the periodic micron ripple double-scale structure, resulting in a decrease in the WCA on the surface of the SSM. The WCA on the surface is still as high as $155.4 \pm 2^\circ$ because of the micro-nano double-scale structure still present on the surface.

The effect of laser scanning speed on SSM morphology and wettability

As shown in Fig. 2, under the same parameters (power density of $5.73 \times 10^6 \text{ W/cm}^2$ and scanning interval of $20 \mu\text{m}$), four groups of parameters with scanning speeds of 100 mm/s, 150 mm/s, 200 mm/s, and 250 mm/s were selected to prepare the superhydrophobic SSM for comparative analysis of the surface morphology and wettability.

Figures 2(a–d) shows the surface morphology of the macro MMS under different laser scanning speeds. The black part of the SSM is the laser processing area, and the processing area is 1 cm^2 . It is obvious from the figure that the black area gradually becomes lighter, which is due to the decreasing energy in the laser processing area, resulting in the decreasing laser removal depth and the increasing reflection of light. Figures 2(a1–a3), (b1–b3), (c1–c3), and (d1–d3) show the SEM images of the laser-ablated SSM at different magnifications at different scanning speeds. As the scanning speed increases, the laser-induced PMRS on the surface of the SSM changes from present to absent, as shown in Fig. 2(a2–d2). As shown in Fig. 2(a3–d3), the formation of PMRS and the deposition of nanoparticles on the SSM can be observed at the scanning speeds of 100 mm/s and 150 mm/s, and the period of the ripple structure is 800 nm–1100 nm. Compared to the untreated [Fig. 2(e1–e3)] SSM surface, the laser-ablated surface formed a micro-nano double-scale structure, which greatly improved its surface roughness. However, at scanning speeds of 200 mm/s and 250 mm/s, the depth of the laser-induced periodic micro-nano double-scale structure surface was reduced or appeared as nanoparticles on the surface.

Figure 2(f) shows the relationship between laser scanning speed and WCA and SA. After in laser ablation and stearic acid modification of the SSM surface, the WCA are more than 145° , with high hydrophobicity, partly reaching superhydrophobicity. The figure shows that the CA increases with increasing scanning speed when the scanning speed is below 150 mm/s. When the scanning speed is 150 mm/s, the surface has the best performance at this time, showing superhydrophobicity with a WCA

of $157.1 \pm 1.5^\circ$ and SA of $3 \pm 0.5^\circ$. From both Fig. 2(a2) and (b2), it can be found that both have periodic micron ripple and micro-nano double-scale structures, but it can also be clearly seen that the grooves between the PMRS in Fig. 2(a2) are too large compared to the structure in Fig. 2(b2), and in the same case, the measured droplets on the surface may appear to penetrate into the grooves, reducing the WCA of the surface and increasing the SA. When the scanning speed exceeds 150 mm/s, the WCA decreases as the scanning speed increases. Few or no PMRS can be seen in Fig. 2(c2–d2); however, in Fig. 2(c3–d3) it can be seen that there are nanoparticles, so there is still a high hydrophobic property on the surface.

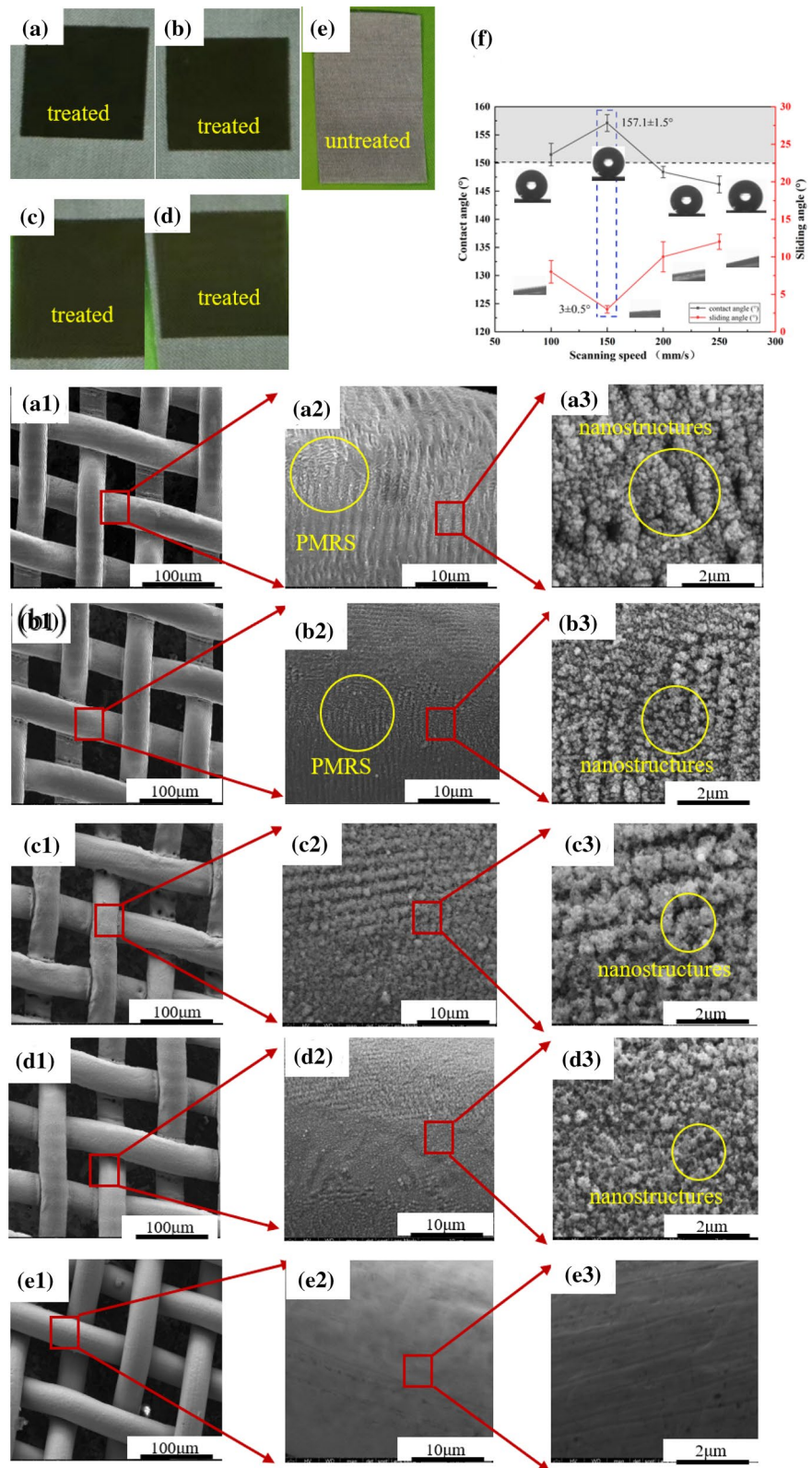
The effect of laser scanning interval on SSM morphology and wettability

As shown in Fig. 3, the morphological and wettability characteristics of laser-ablated SSM surfaces at different scanning intervals ($10 \mu\text{m}$, $20 \mu\text{m}$, $30 \mu\text{m}$, and $40 \mu\text{m}$) were compared and analyzed with the same other parameters (power density of $5.73 \times 10^6 \text{ W/cm}^2$ and scanning speed of 150 mm/s).

Figures 3(a–e) shows the macroscopic morphology with scanning intervals of $10 \mu\text{m}$, $20 \mu\text{m}$, $30 \mu\text{m}$, $40 \mu\text{m}$, and untreated, respectively. As shown in Fig. 3(a–d), the color of the SSM surface decreases from darker to lighter, this is due to the fact that when the scanning interval is small, some of the surface will cause a secondary scan. In the same area of laser irradiation, more number of pulses will lead to different depth of laser ablation and the degree of reflection of light is constantly enhanced, so the surface color is darker. Figures 3(a1–a3), (b1–b3), (c1–c3), and (d1–d3) show the SEM images of the laser-ablated SSM surface at different scanning intervals with different magnifications. The specific differences in morphology cannot be clearly seen in Fig. 3(a1–d1), but the differences in surface structure can be easily seen in Fig. 3(a2–d2) and (a3–d3). With increasing scanning interval, the laser-induced periodic micron ripple structure on the SSM surface changes from present to absent. When the scanning interval is $10 \mu\text{m}$ – $30 \mu\text{m}$, there is a PMRS on the SSM surface, and the period of its ripple structure is about $1 \mu\text{m}$. As shown in Fig. 3(a3–c3), the laser-induced periodic micron ripple structure has nanoparticles on the surface, which greatly increases the surface roughness compared to the untreated [Fig. 3(e1–e3)] SSM surface. However, when the scanning interval is $40 \mu\text{m}$, the surface PMRS is not obvious or absent, but the nanostructure is still present on the surface, as shown in Fig. 3(d3).

As shown in Fig. 3(f), the relationship between different scanning intervals and the CA and SA is explored. As can be seen from the figure, the WCA of the SSM surface exceeds 145° at different scanning intervals, which has excellent hydrophobic properties. When the scanning interval is $10 \mu\text{m}$ – $30 \mu\text{m}$,

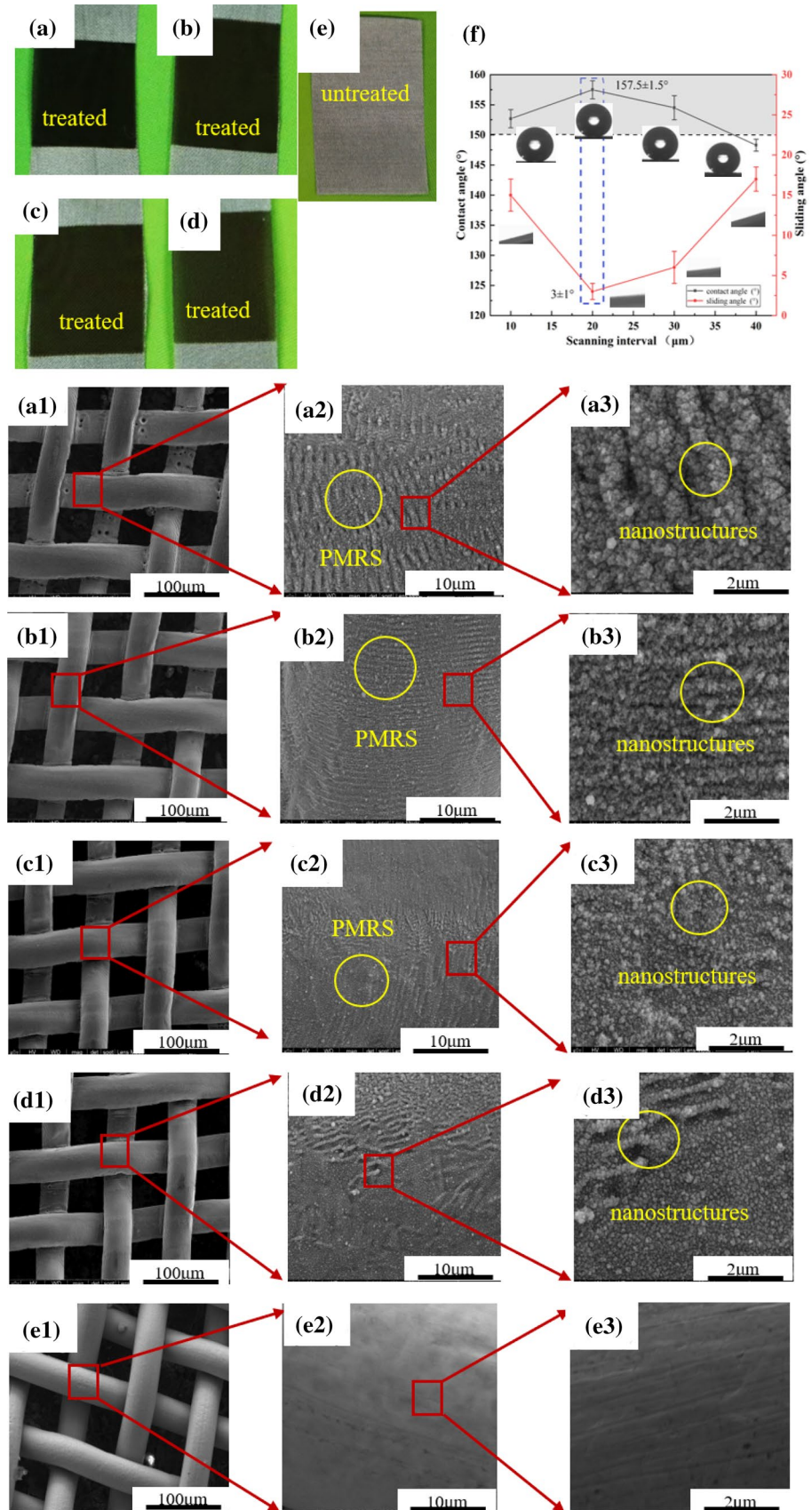
Figure 2: Relationship between scanning speed and surface morphology and WCA. (a–e) Macroscopic surface morphology of laser-ablated SSM at different scanning speeds; (a1–e1), (a2–e2), and (a3–e3) are microscopic SEM of laser-ablated SSM at different scanning speeds with magnifications of $\times 1000$, $\times 10000$, and $\times 50000$, respectively.



the WCA exceeds 150°, when the SSM surface has superhydrophobicity. When the scanning interval is less than 20 μm , the WCA increases with the increase of the scanning interval,

when it reaches 20 μm , the best characteristic of the SSM surface at this time, the WCA is $157.5 \pm 1.5^\circ$ and the SA is $3 \pm 1^\circ$. When the scanning interval is 10 μm –20 μm , the surfaces all

Figure 3: Relationship between scanning interval and surface morphology and WCA. (a–e) Macroscopic surface morphology of laser-ablated SSM at different scanning intervals; (a1–e1), (a2–e2), and (a3–e3) are microscopic SEM of laser-ablated SSM at different scanning intervals with magnifications of $\times 1000$, $\times 10000$, and $\times 50000$, respectively.



have micro-nano double-scale periodic micron ripple structures. However, the width and depth of the grooves between the PMRS are wider and deeper when the scanning interval is 10 μm than when the scanning interval is 20 μm , as can be seen in Fig. 3(a2–b2) and (a3–b3). This causes droplets on the surface to soak into the microstructure, creating a large adhesion force on the surface, decreasing the WCA and increasing the SA. When the scanning interval exceeds 20 μm , the WCA decreases with increasing scanning interval at this time. As shown in Fig. 3(c2–d2), the surface WCA decreases and the SA increases due to the reduction or absence of the PMRS on the surface, but the presence of nanoparticles on the surface can be seen in Fig. 3(c3–d3), and the surface can still surface excellent hydrophobicity after the stearic acid modification.

SSM surface chemical composition analysis

In order to investigate the reaction of the SSM surface and the influence of chemical elements on the wettability of the surface, as shown in Fig. 4, we carried out EDS energy spectroscopy and SEM–EDS spectroscopy measurements on the SSM surface, from the figure found that the surface chemical elements were uniformly distributed on the SSM surface. As shown in Fig. 4(a), the elemental content of the original SSM surface in the elemental content of Fe accounted for 67.28%; C and O content accounted for less; at this time the WCA of the surface is 105.4°, the surface has poor hydrophobic properties. During the picosecond laser ablation process, high temperatures and pressures are generated in the processing area, causing oxides to form on the SSM surface. As shown in the table in Fig. 4(c), the content of C and O on the surface increases and the content of Fe decreases. The brightness of the elements in the elemental spectrograms from Fig. 4(a, c) can also be seen that the content of O increases and the content of Fe decreases, at which time the water contact angle of the surface is 36.7°, with a strong hydrophilicity, which is due to the large surface energy of the surface, making the water droplets directly from the SSM holes. Figure 4(b) shows the energy spectra of the SSM surface after laser processing and stearic acid modification and its elemental distribution spectra. Compared with the Fe and O spectral peaks in Fig. 4(b) and Fig. 4(a, c), it can be clearly found that the elemental peak height of Fe element decreases and that of O element increases. From the elemental content table in Fig. 4(b), we can see that the content of O is much higher than that in Fig. 4(a, c) with a percentage of 29.68%, while the content of Fe is much lower than that in Fig. 4(a, c) with a percentage of 45.27%. It can also be seen from the spectrograms that the O elemental graph in Fig. 4(b) is brighter than the O elemental graph in Fig. 4(a, c), and the Fe elemental graph in Fig. 4(b) is darker than the Fe elemental graph in Fig. 4(a, c). The WCA of the SSM after laser ablation and stearic acid modification was

156.1°, confirming the successful modification of stearic acid on the SSM surface. Experiments performed on the surface of an original SSM immersed in a stearic acid solution yielded a WCA of 115.1°.

Electrochemical property analysis of superhydrophobic SSM

For the SSM in the oil–water separation process, the water environment exists in a complex and diverse situation (which may contain acid, alkali, salt substances), and SSM in this environment for long-term use will lead to a certain degree of corrosion on the surface of SSM, thus affecting the performance and working life of SSM.

Figure 5 shows the dynamic potential polarization curve of SSM in 3.5% NaCl solution, and the specific parameters obtained after linear fitting are shown in Table 1 (Supplementary Information). SSM will develop pitting corrosion in solutions containing Cl^- , which will increase the corrosion efficiency and accelerate the destruction of the surface. In the table, the self-corrosion potentials of untreated and stearic acid-treated SSM mesh are -0.454 V and -0.289 V , respectively; the self-corrosion current densities are $6.32 \times 10^{-6}\text{ A cm}^{-2}$ and $1.25 \times 10^{-6}\text{ A cm}^{-2}$, respectively. In comparison, the self-corrosion potential and self-corrosion current density on the surface of superhydrophobic SSM are significantly higher than those on the surface of untreated SSM, which shows that superhydrophobic SSM has excellent properties in terms of corrosion resistance. Analysis of it causes the existence of a large number of laser-induced periodic micro-nano double-scale structure on the surface of the superhydrophobic SSM, the structure of which stores a large amount of air, making the surface of the SSM to form a layer of air cushion; air cushion as a dielectric prevents the transfer of electrons between the SSM and the electrolyte, reducing the contact between the surface and the corrosive solution; stearic acid will also form a molecular film on the surface to effectively protect the surface of the SSM from corrosive solutions, thereby improving the corrosion resistance of the SSM.

Mechanical and chemical stability analysis of superhydrophobic SSM

Mechanical stability is an important indicator of superhydrophobic SSM in practical applications. The mechanical stability of the material is verified both by testing the wettability of the surface of the superhydrophobic SSM after abrasion. When the WCA of the material surface after testing wear is greater than 150°, the material surface still maintains the superhydrophobic characteristics; when the WCA of the material surface after testing wear is less than 150°, the material surface loses its superhydrophobic characteristic.

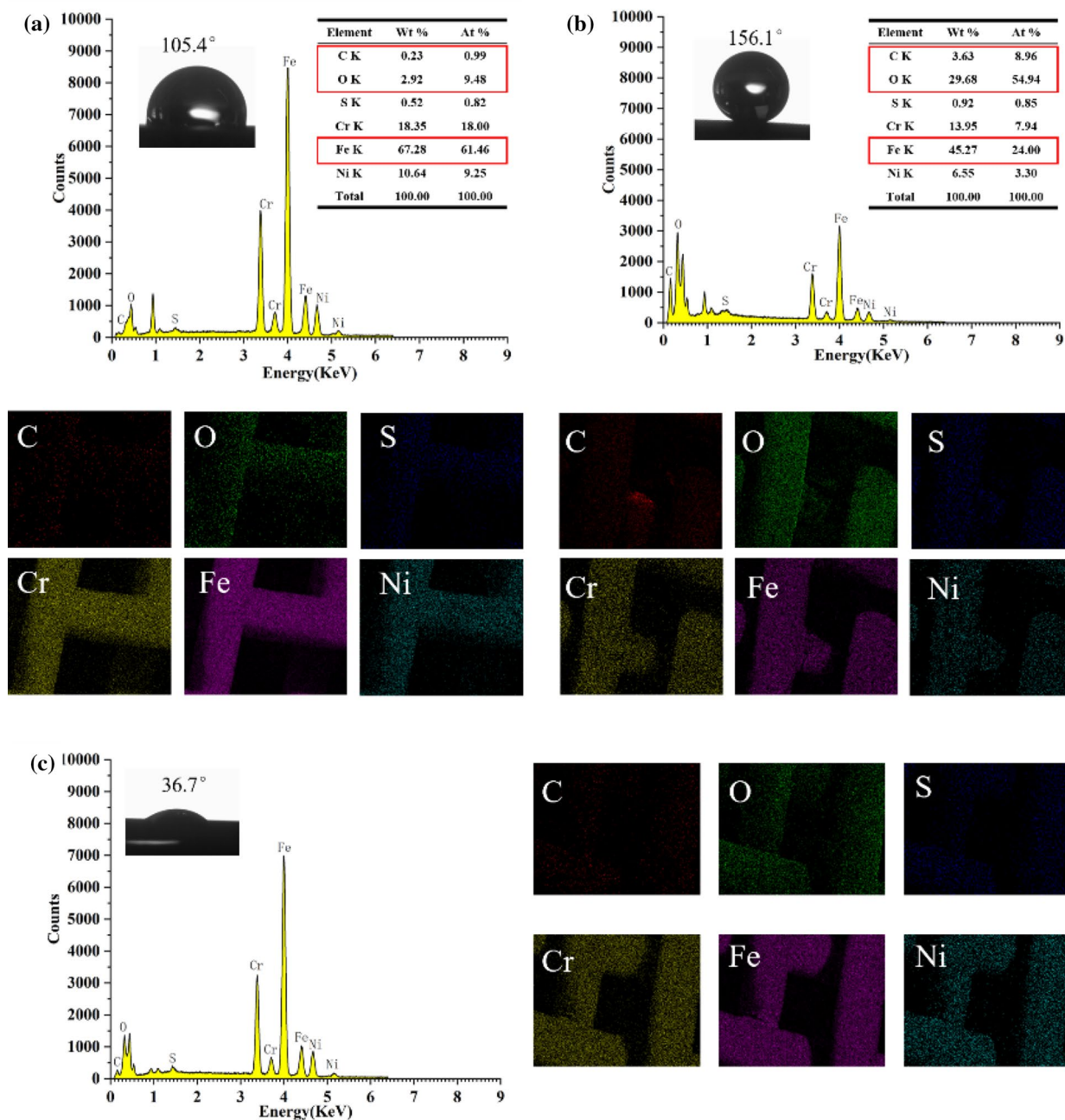


Figure 4: EDS spectra and SEM-EDS spectra of SSM surface. (a) EDS energy spectrum and SEM-EDS spectrum of the original SSM surface; (b) EDS energy spectrum and SEM-EDS spectrum of the SSM surface after laser ablation and stearic acid modification; and (c) EDS energy spectrum and SEM-EDS spectrum of the SSM surface after laser ablation.

Figure 6(a) shows a picture of the SSM grinding device. The superhydrophobic SSM was placed on 1000-mesh sandpaper for abrasion and a 100 g weight was placed on the sample and stretched to 12 cm in one direction to assess the stability of the surface by the WCA of the sample surface after abrasion. As shown in Fig. 6(b), the overall WCA of the worn SSM showed a decreasing trend with the increase of the number of cycles. After 20 cycles of wear, the CA between the SSM and

water decreases from 157.5 ± 1 to $148.6 \pm 2^\circ$, and the WCA of the surface is still above 145° , which indicates that the surface of the superhydrophobic SSM has excellent mechanical properties. As shown in Fig. 6(c-d), some scratches on the surface of the SSM before and after wear can be clearly observed in the figure, and the microscopic morphology of the SSM surface before and after friction is observed using scanning electron microscopy. Figures 6(c1-c2) and (d1-d2)

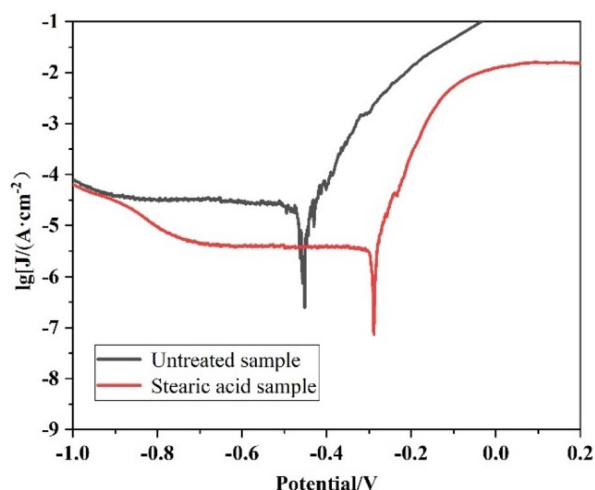


Figure 5: Dynamic potential polarization curves of untreated and stearic acid-modified SSM.

can be observed that the laser-induced periodic micron corrugated structure of the SSM after wear has significant wear, but still has a certain micro-nano rough structure, so it maintains stable mechanical properties before and after friction.

In actual use, in the face of the severe environment that may be encountered, the corrosion resistance of superhydrophobic SSM is an important factor whether it can be used properly. Preparation of pH = 3 HCl solution and 3.5-wt% NaCl solution as acidic and seawater corrosion solution (due to the substance that reduces the surface energy of SSM is stearic acid, which will react with alkali, superhydrophobic SSM is not suitable for testing in alkaline solution), the superhydrophobic SSM is immersed in the corrosion solution and left for 120 h (measure the WCA of SSM surface every 4 h), used to detect the chemical stability of the surface, and to explore the law of WCA change and its corrosion resistance potential.

As shown in Fig. 7(b), the surface WCA of the superhydrophobic SSM immersed in HCl solution and NaCl solution keeps decreasing, before 60 h of immersion, the surface WCA of the superhydrophobic SSM is above 150°, and after 60 h of immersion in HCl solution, SSM WCA is less than 150°; however, it keeps above 145°, while the WCA of the SSM immersed in NaCl solution WCA has been maintained above 150°. The reason for the reduction of the WCA is as the corrosion solution enters part of the stainless steel mesh, oxidation will occur on the WCA wire. On the one hand, the SSM is corroded [Fig. 7(c, d)]; on the other hand, there are also residual NaCl crystals on the surface [Fig. 7(d)], both of which will lead to a reduction in the WCA of the surface. The surface can still maintain the superhydrophobic properties of the reason:

on the one hand, the superhydrophobic SSM surface of the laser-induced periodic micro-nano corrugated double-scale structure stored in a large amount of air, so that the surface of the SSM forms a layer of air cushion, this air cushion is to prevent direct contact between the corrosion solution and the surface of the SSM and to protect the surface of the SSM from corrosion solution; on the other hand, in the process of corrosion of the surface will produce an oxide film, preventing further corrosion of the SSM.

Time-sensitive property testing

In practical applications, the ability of the prepared superhydrophobic SSM surface to have long-term superhydrophobic property in air is very important for its application. Therefore, testing the stability of superhydrophobic SSM for long storage in air needs to be extra important, and the superhydrophobic durability of SSM can reflect its working life. In this experiment, the prepared superhydrophobic SSM is placed in an air environment (among the main parameters of the air in the laboratory are the temperature is maintained at about 25 °C and the air humidity is maintained at 30% HR) and kept at room temperature for 60 days, and the WCA on the superhydrophobic SSM surface is measured every 5 days to investigate whether the surface of the superhydrophobic SSM can maintain superhydrophobicity for a long time.

Figure 8(a) shows the relationship between the WCA and SA of the superhydrophobic SSM surface and the number of days. In the figure, with the increase of the number of days, the WCA shows a decreasing trend and the SA shows an increasing trend. The CA and SA of the surface changed slightly in the first 15 days, but there was almost no change, and the surface of the SSM kept good superhydrophobicity. By day 60, the CA and SA were 151.3° and 8°, respectively. The surface of the superhydrophobic SSM specimens remained excellent superhydrophobicity after 60 days in air. The WCA decreases and the SA increases for this reason. On the one hand, the SSM was placed in the air, the air in the micro-nano particles or dust deposited on the surface of the superhydrophobic SSM, resulting in the specimen surface of the gray layer on the low surface energy alkyl part of the coverage; on the other hand, the surface of the SSM and air contact resulting in part of the SSM surface is oxidized resulting in a slight decrease in the CA and a slight increase in the SA, as shown in Fig. 8(b–d).

Self-cleaning property testing

Self-cleaning is an important feature of superhydrophobic surfaces and excellent self-cleaning is one of the advantages of superhydrophobic materials. Contaminants such as dust and

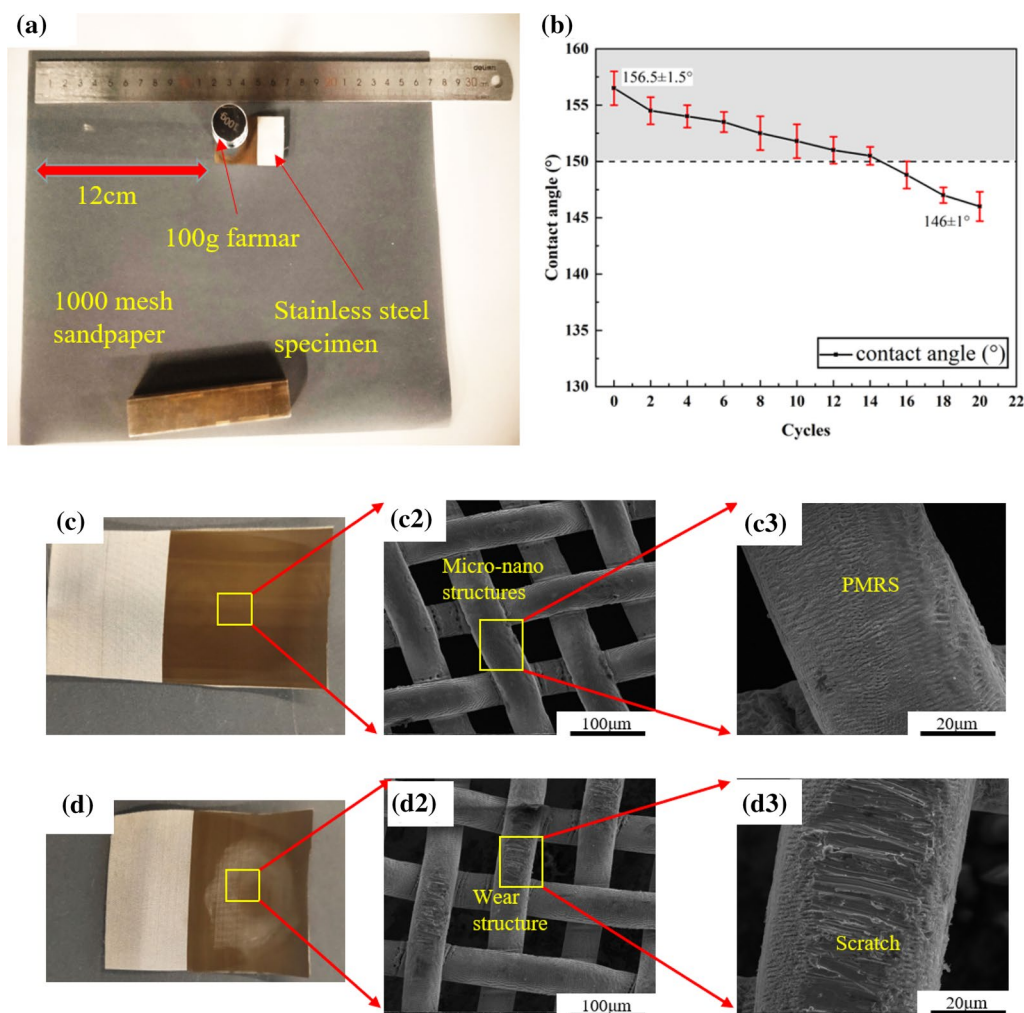


Figure 6: (a) Diagram of the SSM wear device. (b) Relationship between the number of different wear cycles and the WCA of the SSM. (c) Macroscopic morphology of the surface of the SSM before wear. (c1–c2) SEM images of the SSM before wear at $\times 1000$ and $\times 5000$, respectively. (d) Macroscopic morphology of the surface of the specimen after wear. (d1–d2) $\times 1000$ and $\times 5000$, respectively, after wear and $5000\times$ SEM images of the SSM after wear. (d) The macroscopic morphology of the specimen surface after wear. (d1–d2) The SEM images of the SSM after wear at $\times 1000$ and $\times 5000$, respectively.

dirt on the material surface can be washed away by water, which in a sense can represent the lifetime of the material surface. For this purpose, I conducted self-cleaning experiments, and Fig. 9 shows the flowchart for self-cleaning of superhydrophobic SSM surfaces. As shown in Fig. 9(a), the superhydrophobic SSM specimen is placed in a Petri dish and pre-set carbon powder on it; Fig. 9(b–c) shows the liquid droplets were sucked with a microsyringe and made to roll down the surface to take away the carbon powder on the surface. Figure 9(d) shows that as the water droplets roll, the carbon powder is easily washed away and the water droplets do not wet the surface of the SSM. This is due to the micro-nano hierarchical rough structure of the surface of the superhydrophobic SSM will capture a large amount of air, which will play a supporting role for the water droplets that come

into contact with the surface of the SSM. In addition, because the surface of the superhydrophobic SSM has a low surface tension, water droplets in contact with the surface of the SSM is first spread because of inertia and then aggregated to form a spherical shape. The process of spreading and aggregation of water droplets will collect the contaminated debris on the surface of the SSM and then leave the surface of the SSM as the water droplets roll down. As shown in Fig. 9(e), the water droplets immediately adsorbed on the surface of the original SSM specimen upon contact with the surface, and the carbon powder failed to leave the surface of the SSM even after repeated drops of water were added several times. For SSM specimens with superhydrophobic properties, the toner can leave the surface with the water droplets, thus achieving a self-cleaning effect.

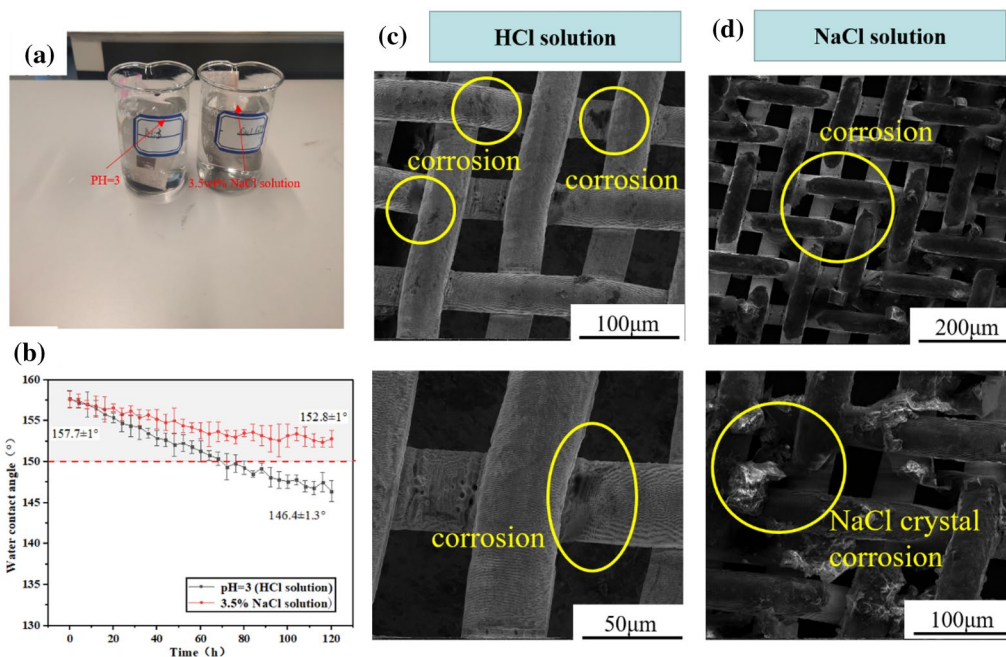


Figure 7: WCA and surface morphology of superhydrophobic SSM immersed in 120 h. (a) Superhydrophobic SSM immersed in pH=3 HCl solution, 3.5-wt% NaCl solution; (b) the relationship between WCA and corrosion time of SSM surface in pH=3 HCl solution or 3.5-wt% NaCl solution; (c) the surface morphology after 120 h of immersion in pH=3 HCl solution; and (d) surface morphology after 120 h of immersion in 3.5-wt% NaCl solution.

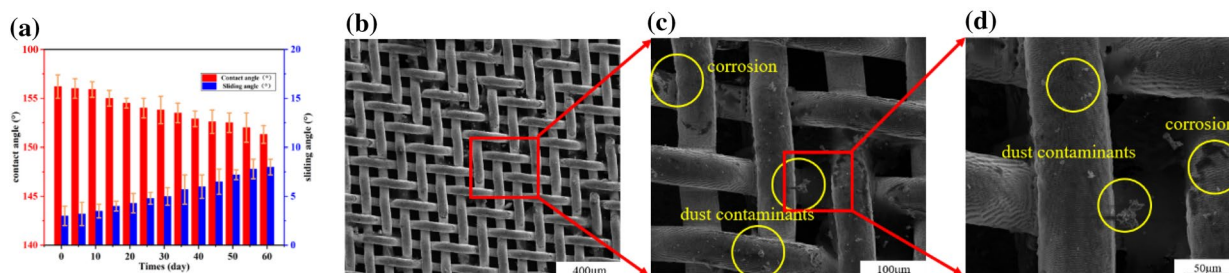


Figure 8: (a) The relationship between WCA and SA of superhydrophobic SSM and the number of days. (b) Surface morphology of superhydrophobic SSM after being placed in air for 60 days. (c) Magnified SEM image of SSM after 60 days in air showing corrosion and dust contaminants. (d) Magnified SEM image of SSM after 60 days in air showing dust contaminants and corrosion.

Conclusion

- (1) The superhydrophobic SSM was prepared by laser ablation of the SSM surface. The optimal process parameters are as follows: power density of 5.73×10^6 W/cm², scanning speed of 150 mm/s, scanning Interval of 20 µm, WCA of 157.5°, and SA of 3°.
- (2) The superhydrophobic SSM surface has a large number of laser-induced periodic micro-nano ripple double-scale structure, which stores a large amount of air in the structure, making the SSM surface form a layer of air cushion, which improves the corrosion resistance of the SSM.

- (3) The superhydrophobic SSM has good mechanical stability, time-sensitive property, and self-cleaning property for the subsequent application to provide a theoretical basis.

Materials and methods

Preparation of superhydrophobic SSM

The experimental material is 316 SSM (300 mesh), which is widely used in the field of oil–water separation because of its excellent corrosion resistance and high separation efficiency. The SSM will be cut into 30 × 30 cm²; first of all, the surface of the SSM is pretreated: it will be put into anhydrous ethanol of

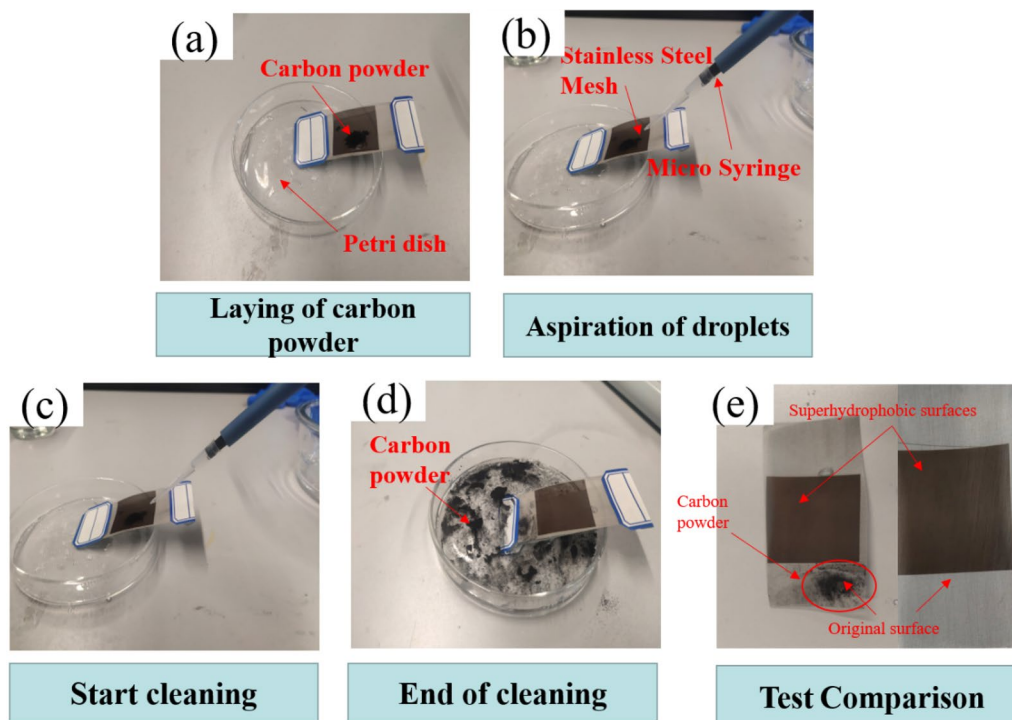


Figure 9: Flowchart for self-cleaning of superhydrophobic stainless steel surfaces.

99.7% purity and cleaned by ultrasonic cleaning equipment for 3–5 min to remove the oil and other debris on the surface of the SSM. Then put into distilled water for ultrasonic cleaning

time of 3 min and finally the cleaned SSM into the vacuum drying oven to dry for use.

The surface with superhydrophobic properties was prepared by scanning the SSM using infrared picosecond laser combined

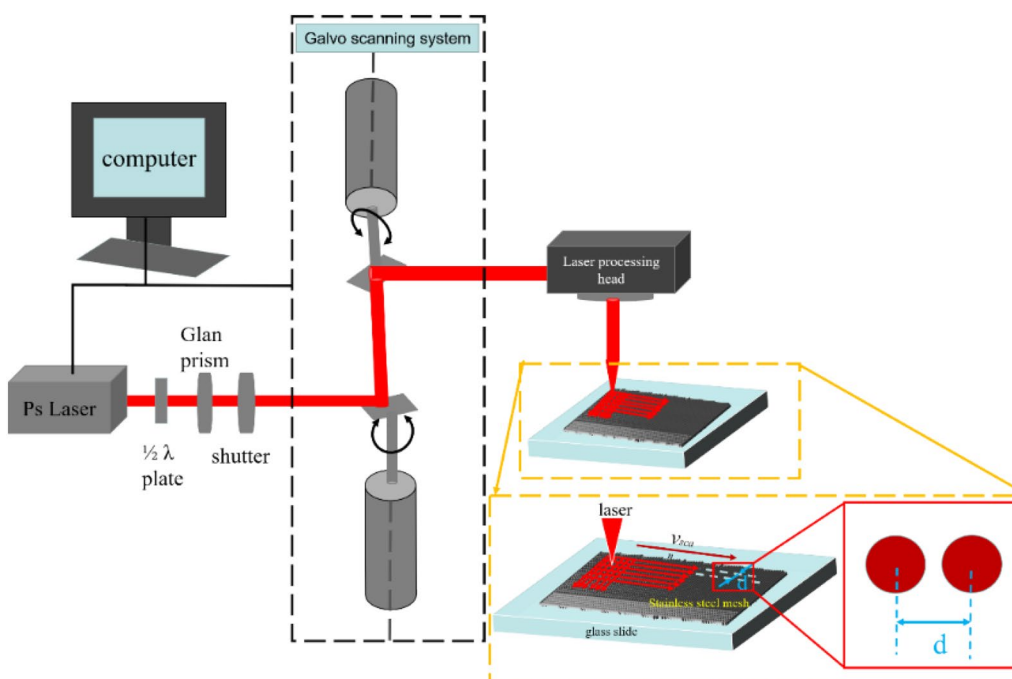


Figure 10: Processing process flowchart.

with stearic acid modification. The processing method is shown in Fig. 10, and the infrared picosecond laser (CTI-WZU-P5040-IR) is provided by Wuxi Chaotong Institute of Intelligent Manufacturing Technology Co. The laser beam used in the laser ablation process has a wavelength of 1064 nm, a repetition frequency of 50 kHz, a pulse width of 10 ps, a maximum power of 30 W, and a focused spot diameter of 20 μm . The picosecond laser scanning route uses a grid-like scanning pattern to ablate the SSM. The process starts with a row scan in the x-direction, followed by a column scan in the y-direction. In the process of laser ablation of SSM surface, the laser power density is changed from $3.82 \times 10^6 \text{ W/cm}^2$ to $6.68 \times 10^6 \text{ W/cm}^2$ ($3.82 \times 10^6 \text{ W/cm}^2$, $4.77 \times 10^6 \text{ W/cm}^2$, $5.73 \times 10^6 \text{ W/cm}^2$, and $6.68 \times 10^6 \text{ W/cm}^2$), the scanning speed is changed from 100 mm/s to 250 mm/s (100 mm/s, 150 mm/s, 200 mm/s, 250 mm/s), and the laser scanning interval is changed from 10 μm to 40 μm (10 μm , 20 μm , 30 μm , 40 μm). Subsequently, the laser-ablated SSM is ultrasonically cleaned in anhydrous ethanol, dried in air, soaked in 0.01 mol L^{-1} stearic acid solution for 2 h, and finally placed in a vacuum drying oven at 200 $^\circ\text{C}$ for 1 h.

Performance testing and characterization methods of materials

The WCA and SA of SSM surface are measured by an optical contact angle meter, which reflects the wettability of the SSM surface to the liquid being measured. Throughout the test phase, the liquid under test is detached from the tip of the microsyringe by gravity and drips onto the surface of the SSM in a volume of 5 μl for each test. When measuring the SA, the platform is tilted at a certain angle so that the droplet rolls off the surface of the material by gravity, at which point the tilt angle of the platform is the SA of the droplet on the surface. To ensure the accuracy of the measurement, this operation was repeated at different 5 positions and finally the values obtained were averaged to obtain the final test results.

FEI's Nova 200 Nano ultra-high resolution field emission scanning electron microscope (SEM) was used to observe the morphology of the original SSM surface, the SSM surface after laser ablation, and the SSM surface after mechanical stability testing and to quantify the elemental composition of the SSM surface under different conditions by the energy dispersive spectroscopy (EDS) system equipped with its equipment.

In order to study the corrosion resistance of the superhydrophobic SSM prepared in this experiment, an electrochemical workstation produced by Shanghai Tatsuwa 660e will be used to characterize the corrosion resistance of the material. The electrochemical workstation can enhance the main control factors without changing the corrosion mechanism in a short time. A standard three-electrode system was used: a platinum sheet as the auxiliary electrode, a saturated glycury electrode as the reference electrode, and a SSM with an area of 1 cm^2 (original surface and superhydrophobic surface) as the working electrode to obtain the kinetic potential polarization curve.

The SSM was placed into the bottom of the epoxy resin for cooling and encapsulation, exposing only the surface under test, ensuring that the contact area between that surface and the test solution was 1 cm^2 . Electrochemical experiments were carried out in 3.5-wt% NaCl solution, and the self-corrosion potential (E_{corr}) and self-corrosion current density (I_{corr}) were obtained by fitting the potentiodynamic polarization curves by software.

Acknowledgments

This research was supported by the Wenzhou Science and Technology Bureau Major Science and Technology Special Project Grant NO. ZG2019002, the Wenzhou Science and Technology Bureau Major Science and Technology Special Project Grant NO. ZG2020029, and the Wenzhou University Rui'an Graduate College of Science and Technology Project No YC202212024.

Author contributions

YZ contributed to writing of the original draft, conceptualization, methodology, visualization, and investigation. YZ contributed to software and data curation. XP contributed to software and data curation. JY contributed to software and data curation. PZ contributed to software and data curation. AF contributed to supervision and validation.

Funding

The Wenzhou Science and Technology Bureau Major Science and Technology Special Project, NO. ZG2019002, Aixing Feng, the Wenzhou Science and Technology Bureau Major Science and Technology Special Project, NO. ZG2020029, Xiaoming Pan, and the Wenzhou University Rui'an Graduate College of Science and Technology Project, YC202212024, Yunhu Zhu

Data availability

The data that support the findings of this study are available from the corresponding author upon reasonable request.

Declarations

Conflict of interest On behalf of all authors, the corresponding author states that there is no conflict of interest.

Ethical approval

This article does not contain any studies with human participants or animals performed by any of the authors.

Supplementary Information

The online version contains supplementary material available at <https://doi.org/10.1557/s43578-023-01038-1>.

References

1. X. Zheng, Q. Zhang, J. Wang, Fabrication of super-hydrophobic magnetic Fe/SiO₂ surface with tunable adhesion inspired by lotus leaf[J]. *Micro & Nano Lett.* **7**(6), 561–563 (2012). <https://doi.org/10.1049/mnl.2012.0335>
2. G. Xuefeng, J. Lei, Water-repellent legs of water striders. *Nature* **432**, 36 (2004). <https://doi.org/10.1038/432036a>
3. S. Pan, M. Chen, L. Wu, Smart superhydrophobic surface with restorable microstructure and self-healable surface chemistry. *ACS Appl. Mater. Interfaces* **12**(4), 5157–5165 (2020). <https://doi.org/10.1021/acsmi.9b22693>
4. H. Ye, L. Zhu, W. Li et al., Constructing fluorine-free and cost-effective superhydrophobic surface with normal-alcohol-modified hydrophobic SiO₂ nanoparticles. *ACS Appl. Mater. Interfaces* **9**(1), 858–867 (2017). <https://doi.org/10.1021/acsmi.6b12820>
5. J. Li, D. Li, Y. Yang et al., A prewetting induced underwater superoleophobic or underoil (super) hydrophobic waste potato residue-coated mesh for selective efficient oil/water separation [J]. *Green Chem.* **18**(2), 541–549 (2016). <https://doi.org/10.1039/c5gc01818h>
6. Y. Li, B. Li, X. Zhao et al., Totally waterborne, nonfluorinated, mechanically robust, and self-healing superhydrophobic coatings for actual anti-icing. *ACS Appl. Mater. Interfaces* **10**(45), 39391–39399 (2018). <https://doi.org/10.1021/acsmi.8b15061>
7. T. Yu, F. Halouane, D. Mathias et al., Preparation of magnetic, superhydrophobic / superoleophilic polyurethane sponge: separation of oil/water mixture and demulsification. *Chem. Eng. J.* **384**, 123339–123347 (2020). <https://doi.org/10.1016/j.cej.2019.123339>
8. H.R. Gao, R.Y. Wang, H.J. Sun et al., Preparations and characterizations of super-hydrophobic surfaces on Al alloys and their anti-icing properties. *Materials in tehnologije* **52**, 299–306 (2018). <https://doi.org/10.17222/mit.2017.125>
9. Y. Zhu, A. Feng, C. Zhang et al., Research on preparation and water collection characteristics of bionic pattern surface for multi-order combination-multi-segment transport. *Opt. Laser Technol.* **156**, 108482 (2022). <https://doi.org/10.1016/j.optlastec.2022.108482>
10. X.N. Zhang, L. Gan, B. Sun et al., Bio-inspired manufacturing of superwetting surfaces for fog collection and anti-icing applications. *Sci. China Technol. Sci.* **65**(9), 1975–1994 (2022). <https://doi.org/10.1007/s11431-022-2101-9>
11. V.S. Saji, Superhydrophobic surfaces and coatings by electrochemical methods—a review. *J. Adhesion Sci. Technol.* (2022). <https://doi.org/10.1080/01694243.2022.2031462>
12. Q. Liu, Y. Tang, W. Luo et al., Fabrication of superhydrophilic surface on copper substrate by electrochemical deposition and sintering process. *Chin. J. Chem. Eng.* **23**(7), 1200–1205 (2015). <https://doi.org/10.1016/j.cjche.2014.11.034>
13. Y. Zhang, Z. Zhang, J. Yang et al., Fabrication of superhydrophobic surface on stainless steel by two-step chemical etching. *Chem. Phys. Lett.* **797**, 139567 (2022). <https://doi.org/10.1016/j.cjche.2014.11.034>
14. S. Ge-Zhang, H. Yang, H. Ni et al., Biomimetic superhydrophobic metal/nonmetal surface manufactured by etching methods: a mini review. *Front Bioeng Biotechnol* (2022). <https://doi.org/10.3389/fbioe.2022.958095>
15. Z. Buczko, K. Olkowicz, J. Krasucki et al., Superhydrophobic properties of aluminium produced by surface abrasive blasting, anodic oxidation and fatty acid impregnation. *Trans IMF* **99**(2), 73–79 (2021). <https://doi.org/10.1080/00202967.2021.1877473>
16. S.F. Ou, K.K. Wang, Y.C. Hsu, Superhydrophobic NiTi shape memory alloy surfaces fabricated by anodization and surface mechanical attrition treatment. *Appl. Surf. Sci.* **425**, 594–602 (2017). <https://doi.org/10.1016/j.apsusc.2017.07.038>
17. Y. Li, X. Zhu, X. Zhou et al., A facile way to fabricate a super-amphiphobic surface. *Appl. Phys. A Mater. Sci. Process* **115**(3), 765–770 (2014). <https://doi.org/10.1007/s00339-014-8438-8>
18. L.S. Solaree, A. Monshi, H. Ghayour, A new approach for the fabrication of hydrophobic silica coatings on glass using sol–gel Method. *Synth. React. Inorg. Met.-Org., Nano-Met. Chem.* **45**(12), 1769–1772 (2015). <https://doi.org/10.1080/15533174.2013.872132>
19. W. Li, X. Tan, J. Zhu et al., Broadband antireflective and superhydrophobic coatings for solar cells[J]. *Mater. Today Energy* **12**, 348–355 (2019). <https://doi.org/10.1016/j.mtener.2019.03.006>
20. Y. Song, C. Wang, X. Dong et al., Controllable superhydrophobic aluminum surfaces with tunable adhesion fabricated by femtosecond laser. *Opt. Laser Technol.* **102**, 25–31 (2018). <https://doi.org/10.1016/j.optlastec.2017.12.024>
21. X. Bai, F. Chen, Recent advances in femtosecond laser-induced superhydrophobic surfaces. *Acta. Optica Sinica* **41**(1), 0114003 (2021). <https://doi.org/10.3788/AOS202141.0114003>
22. X. Li, Y. Jiang, Z. Zhang et al., Facile and environmentally-friendly fabrication of underwater superaerophobic and superaerophilic metallic surfaces through laser ablation and heat treatment. *Coll. Surf. A: Physicochem. Eng. Aspects* **621**, 126547 (2021). <https://doi.org/10.1016/j.colsurfa.2021.126547>
23. J. Huo, Q. Yang, J. Yong et al., Underwater Superaerophobicity/Superaerophilicity and unidirectional bubble passage based on the femtosecond laser-structured stainless steel mesh. *Adv. Mater. Interfaces* **7**(14), 1902128 (2020). <https://doi.org/10.1002/admi.201902128>
24. J. Wang, J. Xu, Z. Lian et al., Facile and green fabrication of robust microstructured stainless steel mesh for efficient oil/water separation via waterjet-assisted laser ablation. *Coll. Surf. A: Physicochem. Eng. Aspects* **643**, 128703 (2022). <https://doi.org/10.1016/j.colsurfa.2022.128703>
25. J. Wang, J. Xu, G. Chen et al., Reversible wettability between underwater superoleophobicity and superhydrophobicity of

- stainless steel mesh for efficient oil–water separation[J]. *ACS Omega* **6**(1), 77–84 (2020). <https://doi.org/10.1021/acsomega.0c03369>
26. Y. Ge, J. Cheng, X. Wang et al., Formation and properties of superhydrophobic Al coatings on steel. *ACS Omega* **6**(28), 18383–18394 (2021). <https://doi.org/10.1021/acsomega.1c02299>
 27. A. Gong, Y. Zheng, Z. Yang et al., Spray fabrication of superhydrophobic coating on aluminum alloy for corrosion mitigation. *Mater. Today Commun.* **26**, 101828 (2021). <https://doi.org/10.1016/j.mtcomm.2020.101828>
 28. J. Zheng, G. Qu, B. Yang et al., Facile preparation of robust superhydrophobic ceramic surfaces with mechanical stability, durability, and self-cleaning function. *Appl. Surf. Sci.* **576**, 151875 (2022). <https://doi.org/10.1016/j.apsusc.2021.151875>
 29. W. Li, Y. Zhan, S. Yu, Applications of superhydrophobic coatings in anti-icing: theory, mechanisms, impact factors, challenges and perspectives. *Prog. Org. Coat.* **152**, 106117 (2021). <https://doi.org/10.1016/j.porgcoat.2020.106117>
 30. M. Yu, X. Li, X. Tan et al., Fluorine-free preparation of superhydrophobic coating with anti-icing property, mechanical durability and self-cleaning effect. *Soft Matter* (2023). <https://doi.org/10.1039/d2sm01265k>
 31. S. Li, M. Cai, Y. Liu et al., S-Scheme photocatalyst TaON/Bi₂WO₆ nanofibers with oxygen vacancies for efficient abatement of antibiotics and Cr (VI): intermediate eco-toxicity analysis and mechanistic insights. *Chin. J. Catal.* **43**(10), 2652–2664 (2022). [https://doi.org/10.1016/S1872-2067\(22\)64106-8](https://doi.org/10.1016/S1872-2067(22)64106-8)
 32. M. Cai, Y. Liu, K. Dong et al., A novel S-scheme heterojunction of Cd₀.5Zn₀.5S/BiOCl with oxygen defects for antibiotic norfloxacin photodegradation: performance, mechanism, and intermediates toxicity evaluation. *J. Coll. Interface Sci.* **629**, 276–286 (2023). <https://doi.org/10.1016/j.jcis.2022.08.136>
 33. C. Wang, R. Yan, M. Cai et al., A novel organic/inorganic S-scheme heterostructure of TCPP/Bi₁₂O₁₇Cl₂ for boosting photodegradation of tetracycline hydrochloride: kinetic, degradation mechanism, and toxic assessment. *Appl. Surf. Sci.* **610**, 155346 (2023). <https://doi.org/10.1016/j.apsusc.2022.155346>
 34. M. Cai, Y. Liu, C. Wang et al., Novel Cd₀.5Zn₀.5S/Bi₂MoO₆ S-scheme heterojunction for boosting the photodegradation of antibiotic enrofloxacin: degradation pathway, mechanism and toxicity assessment. *Sep. Purif. Technol.* **304**, 122401 (2023). <https://doi.org/10.1016/j.seppur.2022.122401>
 35. S. Li, C. Wang, Y. Liu et al., S-scheme MIL-101 (Fe) octahedrons modified Bi₂WO₆ microspheres for photocatalytic decontamination of Cr (VI) and tetracycline hydrochloride: synergistic insights, reaction pathways, and toxicity analysis. *Chem. Eng. J.* **455**, 140943 (2023). <https://doi.org/10.1016/j.cej.2022.140943>
 36. S. Li, M. Cai, C. Wang et al., Ta₃N₅/CdS core-shell S-scheme heterojunction nanofibers for efficient photocatalytic removal of antibiotic tetracycline and Cr (VI): performance and mechanism insights. *Adv. Fiber Mater.* (2023). <https://doi.org/10.1007/s42765-022-00253-5>
 37. S. Li, M. Cai, Y. Liu et al., Constructing Cd₀.5Zn₀.5S/Bi₂WO₆ S-scheme heterojunction for boosted photocatalytic antibiotic oxidation and Cr (VI) reduction. *Adv. Powder Mater.* **2**(1), 100073 (2023). <https://doi.org/10.1016/j.apmate.2022.100073>
 38. M. Cai, C. Wang, Y. Liu et al., Boosted photocatalytic antibiotic degradation performance of Cd₀.5Zn₀.5S/carbon dots/Bi₂WO₆ S-scheme heterojunction with carbon dots as the electron bridge. *Sep. Purif. Technol.* **300**, 121892 (2022). <https://doi.org/10.1016/j.seppur.2022.121892>
 39. Y. Wu, X. Tan, Y. Wang et al., Nonfluorinated, transparent, and antireflective hydrophobic coating with self-cleaning function. *Coll. Surf. A: Physicochem. Eng. Aspects* **634**, 127919 (2022). <https://doi.org/10.1016/j.colsurfa.2021.127919>
 40. R. Wu, S. Wu, H. Jiang et al., Study on corrosion resistance of superhydrophobic surface on aluminum alloy. *Mater. Exp.* **11**(12), 2004–2009 (2021). <https://doi.org/10.1166/mex.2021.2118>
 41. C. Hu, X. Xie, K. Ren, A facile method to prepare stearic acid-TiO₂/zinc composite coating with multipronged robustness, self-cleaning property, and corrosion resistance. *J. Alloys Compd.* **882**, 160636 (2021). <https://doi.org/10.1016/j.jallcom.2021.160636>
 42. J. Zhang, H. Xu, J. Guo et al., A superhydrophobic self-cleaning and anti-icing aluminum sheet fabricated by alkaline solution. *Adv. Eng. Mater.* **23**(10), 2100347 (2021). <https://doi.org/10.1002/adem.202100347>

Publisher's Note Springer Nature remains neutral with regard to jurisdictional claims in published maps and institutional affiliations.

Springer Nature or its licensor (e.g. a society or other partner) holds exclusive rights to this article under a publishing agreement with the author(s) or other rightsholder(s); author self-archiving of the accepted manuscript version of this article is solely governed by the terms of such publishing agreement and applicable law.